Monthly Notices of the ROYAL ASTRONOMICAL SOCIETY

MNRAS **524,** 5514–5523 (2023) https://doi.org/10.1093/mnras/stad2128
Advance Access publication 2023 July 22

Synthetic radio images of structured GRB and kilonova afterglows

Vsevolod Nedora [1,2]★ Tim Dietrich[1,2] and Masaru Shibata[1,3]

[1]*Max Planck Institute for Gravitational Physics (Albert Einstein Institute), Am Mühlenberg 1, Potsdam D-14476, Germany*
[2]*Institute for Physics and Astronomy, University of Potsdam, Potsdam D-14476, Germany*
[3]*Center for Gravitational Physics and Quantum Information, Yukawa Institute for Theoretical Physics, Kyoto University, Kyoto 606-8502, Japan*

Accepted 2023 July 5. Received 2023 June 8; in original form 2023 March 16

ABSTRACT

In this paper, we compute and analyse synthetic radio images of gamma-ray bursts (GRBs) and kilonova afterglows. For modelling the former, we consider GRB170817A-inspired set of parameters, while for the latter, we employ ejecta profiles from numerical-relativity simulations. We find that the kilonova afterglow sky map has a doughnut-like structure at early times that becomes more ring-like at late times. This is caused by the fact that the synchrotron emission from electrons following Maxwellian distribution function dominates the early beamed emission, while emissions from electrons following power-law distribution is important at late times. For an on-axis observer, the image flux centroid moves on the image plane, initially away from the observer. The image sizes, we find, are the largest for equal mass merger simulations with the soft equation of state. The presence of a kilonova afterglow affects the properties inferred from the source sky map, even if the GRB afterglow dominates the total flux density. The main effect is the reduction of the mean apparent velocity of the source, and an increase in the source size. However, this effect becomes negligible around the light curve peak of the GRB afterglow. For a far off-axis observer, neglecting the presence of the kilonova afterglow may lead to systematic errors in the inference of GRB properties from the sky map observations. Notably, at the observing angle inferred for GRB170817A, the presence of kilonova afterglow would affect the sky map properties, only at very late times $t \gtrsim 1500$ d.

Key words: equation of state – gravitational waves – stars: neutron – neutron star mergers.

1 INTRODUCTION

Radio observations have always played an important role in gamma-ray burst (GRBs) studies. Besides complementing the broad-band spectrum analysis, they allow for direct and indirect measurements of the source geometry and dynamics. Specifically, just by using observations of total flux density around the light curves (LCs) peak, it is very challenging to constrain the observing angle, i.e., the angle between the GRBs jet axis and the observer line of sight (LOS). This results in degeneracy among the model parameters Nakar & Piran (2021). Observations of the shift of the radio image centroid allow us to break this degeneracy. However, GRBs jets at cosmological distances are less then a parsec in size and thus their imaging is complicated even with the most sensitive very-long-baseline interferometry (VLBI) facilities. Examples of a successful imaging include GRB030329 and GRB170817A.

GRB030329 was imaged via global VLBI, that reached sub-milliarcsecond (mas) resolution. The image size, approximated with full width at half-maximum (FWHM) (assuming a circular Gaussian model for the image) was 0.07 and 0.17 mas at 23 and 83 d, respectively (Taylor et al. 2004). Multiple observations at different epochs yielded an average expansion of $3 - 5$ c. This superluminal motion hinted at a relativistic expansion of the GRBs jet. This source was also imaged 217 d (Taylor et al. 2005) and 806 d (Pihlstrom et al. 2007) after the original trigger. Combined analysis of the radio images and broad-band data yielded estimates on the jet parameters and its lateral spreading, as well as on the angle beween jet axis and the LOS (Granot, Ramirez-Ruiz & Loeb 2004; Pihlstrom et al. 2007; Mesler et al. 2012; Mesler & Pihlström 2013).

Another example of a successful jet imaging is GRB170817A (Alexander et al. 2017; Savchenko et al. 2017; Troja et al. 2017; Abbott et al. 2017b; Nynka et al. 2018; Hajela et al. 2019), a short GRBs detected by the space observatories *Fermi* (Ajello et al. 2016) and *INTEGRAL* (Winkler et al. 2011), and localized to the S0 galaxy NGC 4993. GRB170817A was an electromagnetic counterpart to the gravitational waves (GWs), even GW170817(Abbott et al. 2017a, 2019a,b). This GRBs was dimmer than other events of its class and was followed by an afterglow, with a prolonged rising part. The most widely accepted explanation for this is that GRB170817A was a structured jet observed off-axis (e.g. Fong et al. 2017; Lamb & Kobayashi 2017; Troja et al. 2017; Alexander et al. 2018; Lamb, Mandel & Resmi 2018; Margutti et al. 2018; Mooley et al. 2018a; Ghirlanda et al. 2019; Ryan et al. 2020). This interpretation is in contrast to the commonly considered uniform jet structure, also called 'top-hat' (Rhoads 1997; Panaitescu & Meszaros 1999; Sari, Piran & Halpern 1999; Kumar & Panaitescu 2000; Moderski, Sikora & Bulik 2000; Granot et al. 2001, 2002; Ramirez-Ruiz & Madau 2004; Ramirez-Ruiz et al. 2005), where energy and momenta do not depend on the angle (outside the jet opening angle). This explanation was in part derived from the analysis of radio images at 75 and 230 d after the burst by the Karl G. Jansky Very Large Array (VLA) and the Robert C. Byrd Green Bank Telescope (Mooley et al. 2018a). The observations showed that the position of the flux centroid has changed between two observational epochs, with the mean apparent velocity along the plane of the sky $\beta_{\rm app} = 4.1 \pm 0.5$. The source, however,

★ E-mail: vsevolod.nedora@aei.mpg.de

remains unresolved. That gave a possible upper limit on the source size of 1 and 10 mas, in the direction perpendicular and parallel to the motion, respectively (Mooley et al. 2018a). The high compactness of the source was further supported by the observed quick turnover around the peak of the radio LCs and a steep decline $F_\nu \propto t_{\rm obs}^{-2}$ after 200 d (Mooley et al. 2018b). Notably, the superluminal motion was also observed in the optical band (Mooley, Anderson & Lu 2022). Ghirlanda et al. (2019) also obtained a radio image at 207 d, confirming the previous findings. Together with the analysis of multiwavelength LCs, the information obtained from radio images allowed to confirm that GRB170817A was produced by a narrow, core-dominated jet rather than by a wide, quasi-isotropic ejecta (Gill & Granot 2018; Hotokezaka et al. 2018). A comparison with GRBs030329, where no proper motion was observed, only the expansion speed, indicates that the main differnece lies in a viewing angle.

A sizable fraction of GRBss occurs further off-axis than GRB170817A. For them, the prompt gamma-ray emission, as well as early afterglow may not be seen, as they would be beamed away from the observer's LOS. At later times, however, as the jet decelerates and spreads laterally, the afterglow should become visible. Such afterglow is referred as 'orphan afterglow' (Rhoads 1997). And while there have been candidates for such transient (see e.g. Bradley Cenko et al. 2015), no such afterglow has been unumbigously detected so far, despite extensive search campaigns in X-ray (Woods & Loeb 1999; Nakar & Piran 2003), optical (Dalal, Griest & Pruet 2002; Nakar, Piran & Granot 2002; Totani & Panaitescu 2002; Rhoads 2003; Rau, Greiner & Schwarz 2006), and radio (Perna & Loeb 1998; Levinson et al. 2002; Gal-Yam et al. 2006; Soderberg, Nakar & Kulkarni 2006; Bietenholz et al. 2014) (see also Huang et al. 2020).

In addition to GRBs and its afterglow, GW170817 was accompanied by a quasi-thermal electromagnetic counterpart, kilonovae (kNe) AT2017gfo (Arcavi et al. 2017; Coulter et al. 2017; Drout et al. 2017; Evans et al. 2017; Hallinan et al. 2017; Kasliwal et al. 2017; Nicholl et al. 2017; Smartt et al. 2017; Soares-Santos et al. 2017; Tanvir et al. 2017; Troja et al. 2017; Lyman et al. 2018; Mooley et al. 2018a; Ruan et al. 2018). The ejecta responsible for the kNe was enriched with heavy elements, lanthinides, and actinidies, produced via *r*-process nucleosynthesis (Lattimer & Schramm 1974; Li & Paczynski 1998; Kulkarni 2005; Rosswog 2005; Metzger et al. 2010; Roberts et al. 2011; Kasen, Badnell & Barnes 2013; Tanaka & Hotokezaka 2013). The angular and velocity distributions of these ejecta are quite challenging to infer due to the complex atomic properties of these heavy elements. Nevertheless, at least two ejecta components to account for the observed LCs were needed: a lanthanide-poor (for the early blue signal) and a lanthanide-rich (for the late red signal) one (Cowperthwaite et al. 2017; Perego, Radice & Bernuzzi 2017; Tanaka et al. 2017; Tanvir et al. 2017; Villar et al. 2017; Kawaguchi, Shibata & Tanaka 2018; Coughlin et al. 2019). A fit of AT2017gfo LCs to a semianalytical two-components spherical kNe model yielded blue (red) components of mass $2.5 \times 10^{-2}\,{\rm M}_\odot$ ($5.0 \times 10^{-2}\,{\rm M}_\odot$) and velocity 0.27 c (0.15 c) (Cowperthwaite et al. 2017; Villar et al. 2017). The estimated ejecta mass and velocity could be significantly modified if anisotropic effects are taken into account (Kawaguchi et al. 2018).

numerical relativity (NR) simulations of binary neutron star (BNS) mergers predict that mass ejection can be triggered by different mechanisms acting on different time-scales (see Shibata & Hotokezaka 2019; Bernuzzi 2020; Metzger 2020; Radice, Bernuzzi & Perego 2020, for reviews on various aspects of the problem). Specifically, dynamical ejecta of mass $\mathcal{O}(10^{-4} - 10^{-2})\,{\rm M}_\odot$ can be launched during mergers at average velocities of $0.1 - 0.3$ c, e.g. (Rosswog et al. 1999; Rosswog 2005; Bauswein, Goriely & Janka 2013; Hotokezaka et al. 2013a; Wanajo et al. 2014; Sekiguchi et al. 2015; Radice et al. 2016; Sekiguchi et al. 2016; Vincent et al. 2020; Zappa et al. 2022; Fujibayashi et al. 2023). After the merger, quasi-steady state winds were shown to emerge from a post-merger disc (Dessart et al. 2009; Metzger & Fernández 2014; Perego et al. 2014; Fernández et al. 2015; Just et al. 2015; Kasen, Fernández & Metzger 2015; Martin et al. 2015; Wu et al. 2016; Siegel & Metzger 2017; Fahlman & Fernández 2018; Fujibayashi et al. 2018; Metzger, Thompson & Quataert 2018; Fernández et al. 2019; Miller et al. 2019; Nedora et al. 2019; Fujibayashi et al. 2020; Nedora et al. 2021b).

NR simulations also show that a small fraction of dynamical ejecta ($\sim(10^{-6} - 10^{-5})\,{\rm M}_\odot$) has velocity exceeding $\simeq$0.6 c (Hotokezaka et al. 2013b; Metzger et al. 2015; Hotokezaka et al. 2018; Radice et al. 2018a,b; Nedora et al. 2021a; Fujibayashi et al. 2023). Such a fast ejecta are capable of producing bright non-thermal late-time afterglow-like emission, with spectral energy distribution peaking in radio band (e.g. Nakar & Piran 2011; Piran, Nakar & Rosswog 2013; Hotokezaka & Piran 2015; Hotokezaka et al. 2018; Radice et al. 2018b; Desai, Metzger & Foucart 2019; Kathirgamaraju et al. 2019a; Nakar 2020; Nathanail et al. 2021; Hajela et al. 2022). The mechanisms behind the fast tail of the ejecta is not yet clear. Possible options include shocks launched at core bounce (Hotokezaka et al. 2013b; Radice et al. 2018b) and shocks generated at the collisional interface between neutron stars (NSs) (Bauswein et al. 2013). It is important to point out that at present NR simulations cannot capture all the ejection mechanisms and do not include all the physical processes, that may lead to the formation of fast outflows (see e.g. Beloborodov, Lundman & Levin 2020).

Notably, despite a large amount of BNS NR simulations, there is no robust relationship between the binary parameters NSs and NS equation of state (EOS) and the properties of the ejected matter. And while there exist fitting formulae of various complexity to the properties of the bulk of the ejecta, e.g., mass and velocity (Dietrich & Ujevic 2017; Radice et al. 2018b; Dietrich et al. 2020; Krüger & Foucart 2020; Nedora et al. 2022b), even such formulae for the fast ejecta tail are currently absent. Thus, we are limited to employing published dynamical ejecta profiles from NR simulations.

In Nedora et al. (2021a), (hereafter N21), we showed how a kNe afterglow emission from the fast tail of the dynamical ejecta may contribute to the radio LCs of the GRB170817A, employing NR-informed ejecta profiles (Nedora et al. 2019; Perego, Bernuzzi & Radice 2019; Bernuzzi 2020; Nedora et al. 2021b). In Nedora et al. (2022a) (hereafter N22A), we modified the afterglow model by including an additional electron population that assumes Maxwellian distribution in energy behind the kNe blast waves (BWs) shock. We showed that the radio flux from these 'thermal electrons' can be higher than the radio flux from commonly considered 'power-law' electrons at early times, and if ejecta is sufficiently fast. It is thus natural to investigate, whether the emission from thermal electrons affects the radio image of the source. As in N22A, we consider a GRB170817A-inspired GRBs afterglow model of a structured jet, seen off-axis, while for kNe afterglow we consider NR-informed ejecta profiles, extracted from NR simulations, with various NS EOSs and system mass ratios.

The paper is organized as follows. In Section 2, we recall the main assumptions and methods used to calculation the observed GRBs- and kNe- afterglow emission, as well as how to compute the sky map. In Section 3.1, we present and discuss the kNe afterglow sky maps, focusing on the overall properties, e.g., image size and the flux centroid position and their evolution. In Section 3.2, we consider both GRBs and kNe afterglow and discuss how the properties of the former change, when the later is included in the modelling. In

Section 3.3, we briefly remark on how the GRBs plus kNe sky map changes if the interstellar medium (ISM) in front of the kNe ejecta has been pre-accelerated and partially removed by a passage of the laterally spreading GRBs ejecta. Finally, in Section 4, we provide the discussion and conclusion.

2 METHODS

In order to compute the GRBs and kNe afterglows, we employ the semianalytic code PYBLASTAFTERGLOW, discussed in N22A and N21. In the model, both ejecta types are discretized into velocity and angular elements, for each of which the equations of BWs evolution are solved independently, and the synchrotron radiation is computed, accounting for relativistic and time-of-arrival effects. The effect of the pre-processing of ISM medium by a passing GRB BW is considered in Section 3.3, otherwise this effect is not included, and kNe BWs evolved independently from the GRB BWs. The GRB BW lateral expansion is included via an approximate analytical formula that initializes the expansion, once BW has sufficiently decelerated. For kNe afterglow, both thermal and non-thermal electron populations are considered, while for GRB afterglow only the latter is employed in the model. Due to the approximate nature of a semianalytic model, in this work, we need to focus on the qualitative and more general quantitaitve analysis.

The sky maps are computed using the spherical coordinate system discussed in section 2 in N22A (figure 1). For both ejecta types axial symmetry is assumed. Then, each elemental BWs has radial coordinate R_{ij}, and angular coordinates θ_i and ϕ_{ij}, where the single index of θ_i reflects the axial symmetry. The coordinate vector of the elemental BW is given by $\vec{v}_{ij} = R_{ij}\left(\sin(\theta_i)\cos(\phi_{ij})\vec{x},\ \sin(\theta_i)\sin(\phi_{ij})\vec{y},\ \cos(\theta_i)\vec{z}\right)$. The cosine of the angle between the LOS and $\vec{v}_{ij}$ reads,

$$\mu_{ij} = \sin(\theta_i)\sin(\phi_{ij})\sin(\theta_{\rm obs}) + \cos(\theta_i)\cos(\theta_{\rm obs})\,. \quad (1)$$

The image plane, xz is perpendicular to the LOS of the observer. We chose the basis with which the principal jet moves in the positive $\tilde{x}$-direction. The basis vectors then $\tilde{\vec{x}}_{ij} = \sin(\theta_{\rm obs})\vec{z}_{ij} - \cos(\theta_{\rm obs})\vec{x}_{ij}$, $\tilde{\vec{y}}_{ij} = \vec{x}_{ij}$ of the plane as in Fernández, Kobayashi & Lamb (2021), and the coordinates of the ij BW on the image plane (for the principle jet) are given by

$$\begin{aligned}\tilde{x}_{ij} &= -R_{ij}[\cos(\theta_{\rm obs})\sin(\theta_i)\sin(\phi_{ij}) \\ &\quad + \sin(\theta_{\rm obs})\cos(\theta_i))], \\ \tilde{z}_{ij} &= R_{ij}\sin(\theta_i)\cos(\phi_{ij})\,. \end{aligned} \quad (2)$$

In the following, we omit the use of tildas for simplicity.

In order to characterize sky maps we consider the following main quantities. Specifically, following Zrake, Xie & MacFadyen (2018); Fernández et al. (2021), we compute the surface brightness-weighted centre of the image, image centroid, defined as

$$x_{\rm c} = \frac{1}{\int I_\nu {\rm d}x{\rm d}z}\int x I_\nu {\rm d}x{\rm d}z, \quad (3)$$

where I_ν is computed via equation (37) in N22A. We also compute the X and Z-averaged brightness distributions

$$\begin{aligned} I_{\nu;{\rm m}}(x) &= \frac{1}{\Delta z}\int I_\nu(x,z){\rm d}z\,, \\ I_{\nu;{\rm m}}(z) &= \frac{1}{\Delta x}\int I_\nu(x,z){\rm d}x\,. \end{aligned} \quad (4)$$

As the available ejecta profiles are limited in the angular resolution, which severely limits the accuracy of the sky map analysis, we 'rebin' the angular ejecta distribution histograms. To do this rebinning, we assume a uniform distribution within each bin (Knoll 2000).

3 RESULTS

For an extended source with uniform Lorentz factor (LF) Γ, the maximal apparent velocity $\beta_{\rm app} < \Gamma$, while the image size increases with Γ (Boutelier, Henri & Petrucci 2011). A spherically symmetric source that expands isotropically, would appear as a ring expanding with Γ with no motion in the image centroid.

Due to non-trivial ejecta angular and velocity structure a kNe sky map shape, size and structure have a complex dependency on the observer time $t_{\rm obs}$ and angle $\theta_{\rm obs}$. Moreover, if both, thermal and non-thermal electron populations are present behind the shock, there is a non-trivial dependency on the microphysical parameters and ISM density. It is beyond the scope of this work to study all possible combinations of free parameters. Instead, we focus on several representative cases.

Specifically, we fix the source to be located at luminosity distance, $D_{\rm L} = 41.3$ Mpc with redshift $Z = 0.0099$. The micropthysics parameters are the following. Fractions of the shock energy that goes into electron acceleration and magnetic field amplification are $\epsilon_e = 0.1$, $\epsilon_b = 0.001$, and $\epsilon_t = 1$. The slope of the power-law electron distribution is $p = 2.05$. Unless stated otherwise, the observational frequency is 1 GHz, and the observer angle is 45 °. We focus on two $n_{\rm ISM}$: the fiducial value $n_{\rm ISM} = 0.05$ cm^{-3} and $n_{\rm ISM} = 0.00031$ cm^{-3}, that under the aforementioned assumptions regarding the jet structure and microphsycis paramerts leads to a good fit to the GRB170817A afterglow data.

3.1 Kilonova afterglow sky maps

We begin by considering the BNS merger simulation with BLh EOS and $q = 1.00$. The sky map for $\theta_{\rm obs} = 45$ °, $\nu_{\rm obs} = 1$ GHz, and $t_{\rm obs} = 120$ d, after merger is shown in Fig. 1.

At $t_{\rm obs} = 120$ d, the kNe afterglow at 1 GHz for this BNS merger model is dominated by the emission from thermal electron population behind shocks. The fast tail of the dynamical ejecta in this simulation is predominantly equatorial, confined to $\gtrsim$60 ° (see Fig. 3 in N21) with mass-averaged half-root mean square (RMS) angle $\theta_{\rm RMS} \simeq 70$ °. As $\theta_{\rm RMS} > \theta_{\rm obs}$, the synthetic image resembles a wheel with the brightest parts offset from the centre into the negative half of the x-axis, i.e., $x_{\rm c} < 0$. (See $\theta_{\rm obs} = 15$ ° and $\theta_{\rm obs} = 45$ °. subpanels in Fig. 1). An observer with $\theta_{\rm obs} \gtrsim \theta_{\rm RMS}$ would, however, be able to see the beamed emission from the fast ejecta tail (bright spots at $x \simeq 0$ mas, $z \simeq \pm 0.3$ mas on $\theta_{\rm obs} = 75$ °. sub-panels of Fig. 1). Correspondingly, the image flux centroid lies near $x_{\rm c} \simeq 0$, and the brightest part of the image laying in $x > 0$ plane.

As the kNe BWs propagates through the ISM, the size of a sky map increases in both x and z directions. Due to the axial symmetry of the ejecta properties, $\theta_{\rm obs}$ and relativistic effects primarily affect the FWHM$_x$ and $x_{\rm c}$. The example of a sky map evolution is shown in Fig. 2. Deceleration of kNe BWs reduces the contribution from thermal electron population to the observed flux. Additionally, relativistic effects become increasingly less important. Consequently, the image becomes more spherically symmetric and centred around $x_{\rm c} = z_{\rm c} = 0$. Specifically for this simulation, at $t_{\rm obs} = 600$ d after the merger the emission from equatorial and polar BWs becomes comparable with each other and thereafter the sky map resembles a circle with two bright spots near the image's outer boundaries on the $x = 0$ axis. These spots mark the geometrically overlapping emitting areas and reflect the equatorial nature of the ejecta fast

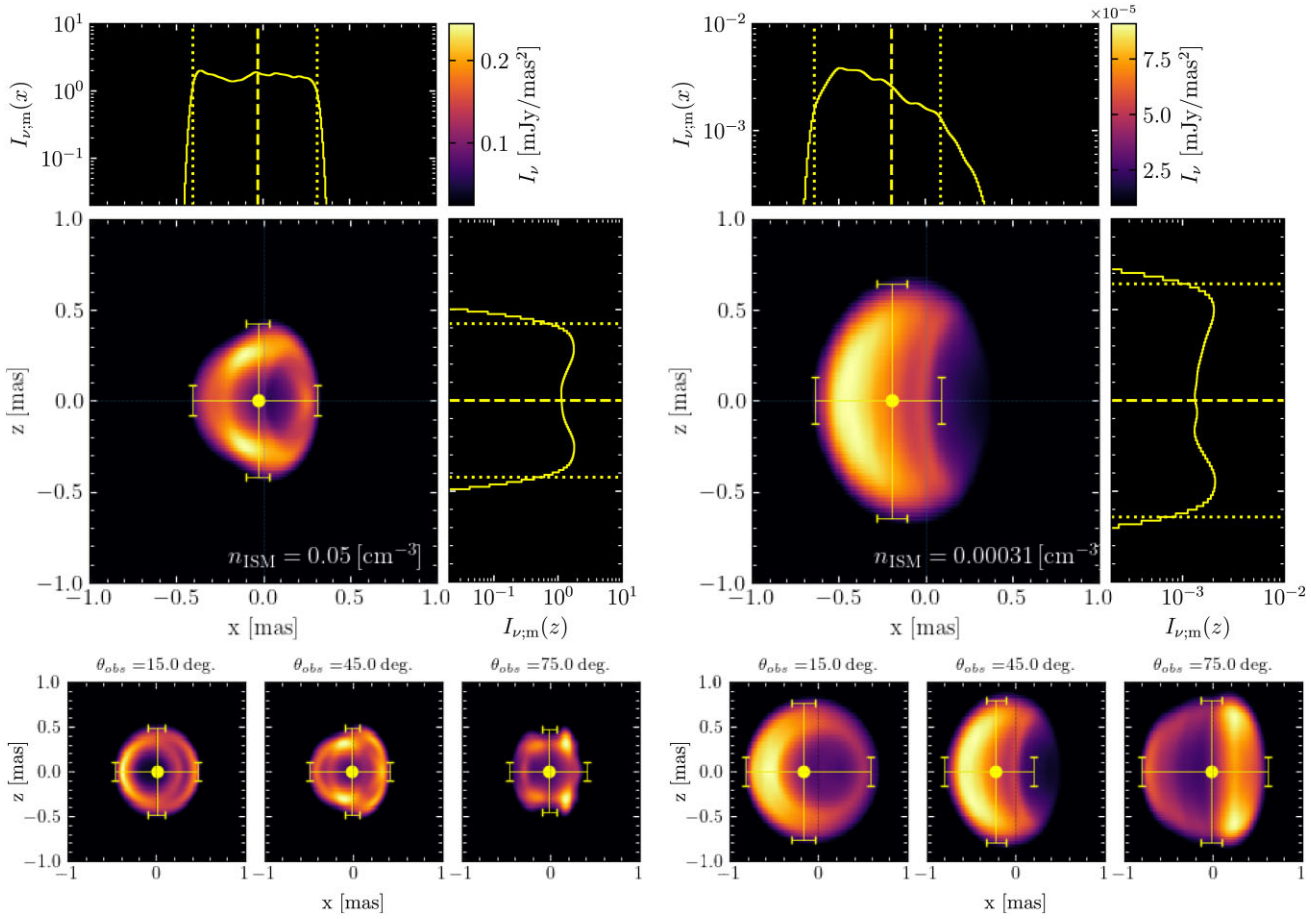

Figure 1. Top figure: sky map for a BNS merger simulation with BLh EOS and $q = 1.00$ computed at 120 d, after the merger at $\nu = 1$ GHz, and observed at $\theta_{\rm obs} = 45^\circ$. Left and right columns of plots corresponds to different ISM densities, $n_{\rm ISM} = 0.05$ cm^{-3} on the left and $n_{\rm ISM} = 0.00031$ cm^{-3} on the right. In each plot column, the top and top-right subplots display the X and Z averaged brightness distributions, respectively. Dotted lines mark FWHM and dashed lines mark the location of the flux centroid of the image. FWHM and the location of the flux centroid are also shown on the main panel of the figure as error bars and the circular marker, respectively. Thin grey dotted lines indicate the X- and Z-axis. Notably, we are plotting $I_\nu/I_{\nu;\,\rm max} \in (0.1, 1)$ range of the normalized specific intensity in order to resolve the image structure more clearly. Bottom panel: same sky map but viewed at three difference angles, $\theta_{\rm obs}$.

tail. Notably, the presence of thermal electrons that we assume in our model does not affect this qualitative picture, as the emissivity from both thermal and non-thermal electron populations depend on the shock velocity albeit to a different degree (e.g. Ozel, Psaltis & Narayan 2000; Margalit & Quataert 2021).

The presence of two electron populations behind BW shocks, however, implies a spectral evolution of the emission in every pixel of the sky map. We define a sky map spectral index as $A_\nu = {\rm dlog}_{10}(I_\nu)/{\rm dlog}_{10}(\nu)$ and show its evolution in Fig. 3 for $\theta_{\rm obs} = 45^\circ$. and $\nu = 1$ GHz. At early times, most of the sky map displays relatively low $A_\nu \simeq -1.25$, indicative of the emission from thermal electron populations (figure 3 in N22A). As the BWs decelerate and emission from the thermal electron population subsides. At the point where the spectrum transitions, the spectral index reaches a minimum. After that, the spectral index rises as the sky map becomes increasingly dominated by emission from the non-thermal electron population. At very late times the spectral map becomes uniform, as the emission from power-law electrons with fixed distribution slope p dominates in every pixel. If resolved in observations, such evolution of the spectral sky map would allow a detailed study of the ejecta velocity and angular distribution, besides constraining the physics of particle acceleration at mildly relativistic shocks.

It is interesting to examine the evolution of the key sky map properties, image size FWHM$_x$, and the position of the flux centroid, $x_{\rm c}$, at very low ISM density, that was generally inferred for GRB170817A. In Fig. 4, we show the evolution of the FWHM$_x$ and $x_{\rm c}$ as well as these values at the peak time t_p of the respective LCs. The sky map size at a given epoch is primarily determined by the energy budget of the ejecta. Simulations with $q = 1$ and soft EOS, e.g., SFHo and SLy4 EOS display larger image sizes throughout the evolution. On the other hand, equal mass simulations with stiffer EOS, such as BLh and LS220 EOSs demonstrate smaller image sizes, More asymmetric binaries display in general intermediate image sizes.

At the time of the LC peak, the image size depends on whether the emission from thermal or non-thermal electron population dominates the observed flux. If former is true, t_p is generally small, $t_p < 500$ d for our simulations and assumed $n_{\rm ISM} = 0.00031$ cm^{-3}, and the image size case does not exceed 4 mas. Notably, at higher $n_{\rm ISM}$ t_p is shorter and thus, the FWHM$_x$ is smaller. Simulations with $q = 1.00$ and soft (SLy4 and SFHo) EOSs are examples of that. If the emission from power-law electrons dominates the observed flux at the time of the LC peak, the image size is significantly larger, $\simeq 15 - 20$ mas. Importantly, t_p depends also on the observer angle $\theta_{\rm obs}$ due to relativistic beaming of the early-time emission

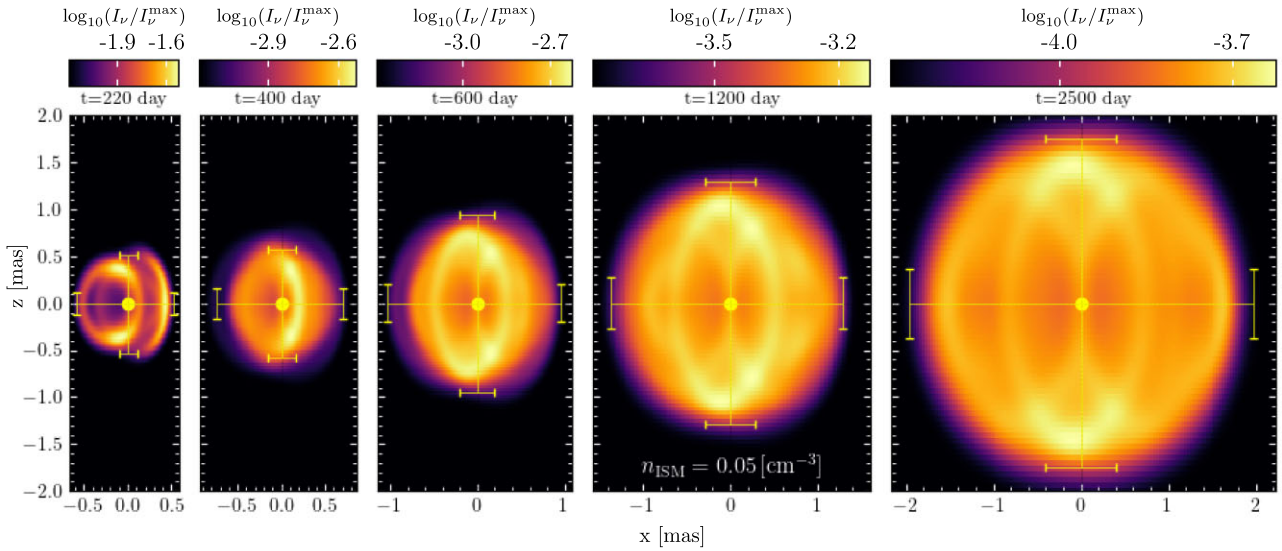

Figure 2. Evolution of the sky map for the BNS merger simulation with BLh EOS and $q = 1.00$, observed at $\theta_{\rm obs} = 45^\circ$, $\nu_{\rm obs} = 1$ GHz. The ISM density is $n_{\rm ISM} = 0.05$ cm^{-3}. As in Fig. 1, the marker and the error bar indicate the location of the flux centroid and the FWHM of the image, while grey dotted lines mark the axis.

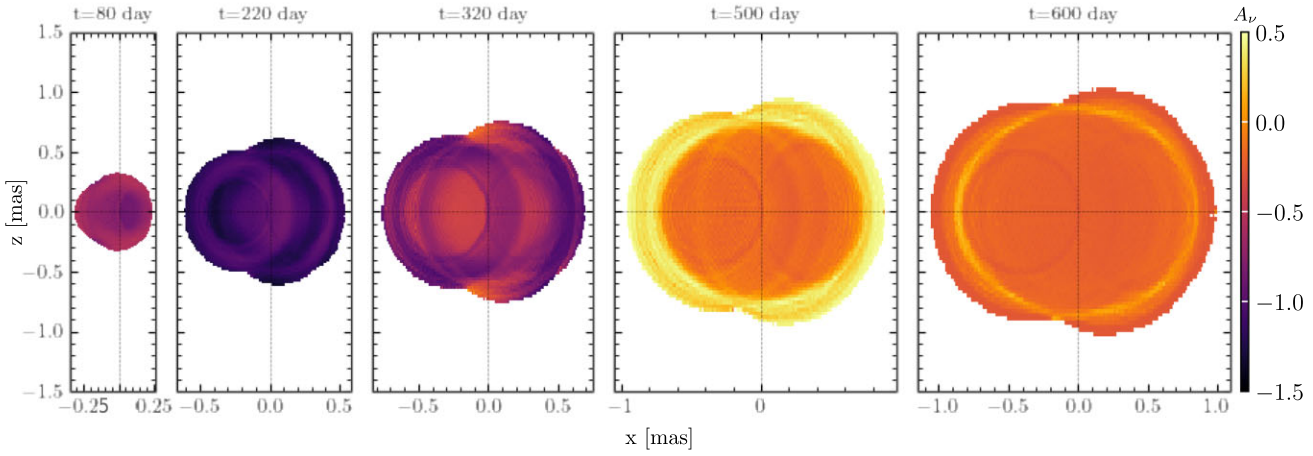

Figure 3. Evolution of the sky map spectral index for the BNS merger simulation with BLh EOS and $q = 1.00$, observed at $\theta_{\rm obs} = 45^\circ$. and at $\nu = 1$ GHz. Here $n_{\rm ISM} = 0.05$ cm^{-3}. Thin dotted lines mark the axis. For clarity, we did not apply the Gaussian smoothing kernel to this image.

from thermal electrons. For example, a simulation with a sufficiently spherically symmetric distribution of the fast tail, simulation with SLy4 EOS and $q = 1.00$ display an early $t_p < 500$ d, at all three observing angles considered.

A characteristic feature of the changing dominant contributor (e.g., electron population) to the observed emission is seen here as a sharp increase in the evolution of image size (sub-panel in the top left panel in Fig. 4). This rapid increase in FWHM$_x$ occurs when the emission from fast BWs, dominating the observed flux at first, subsides and less beamed, more isotropic emission from non-thermal electrons becomes equally important.

As discussed before, the evolution of the image flux centroid position, $X_{\rm c}$, besides the ejecta energy budget, depends strongly on the observational angle. At $\theta_{\rm obs} = 45^\circ$. for BNS merger models with sufficiently fast and equatorial fast tail, $x_{\rm c}$ is negative at an early time (e.g., for simulation with BLh EOS and $q = 1.00$). For simulations with $\theta_{\rm RMS} < \theta_{\rm obs}$, $x_{\rm c}$ moves into the positive half of x-axis at the beginning, as is the the case for the equal mass simulations with SFHo, SLy4 and LS220 EOSs. The time evolution of the $x_{\rm c}$ in most cases exhibits an extremum after which $x_{\rm c} \to 0$. We find that the time of the extremum corresponds to the time where the spectral index evolution of the LC reaches minimum (see figure 4 in N22A for the LC spectral index evolution). In the top right panel of Fig. 4, this point is shown with square marker.

At the time of the LC peak, the position of the flux centroid is generally determined by whether the thermal or non-thermal electrons dominate the observed flux. This in turn depends on $\theta_{\rm obs}$. In the former case $|x_{\rm c}|$ tends to be larger, reaching $|x_{\rm c}| \leq 0.5$ mas, as bright beamed emission from thermal electrons in fast BWs makes the image very asymmetric. Consequently, if the LC peaks at late times, $|x_{\rm c}|$ is closer to zero for most models.

3.2 kN and GRB skymaps

One of the key observables of GRB170817A that confirmed the jetted nature of the outflow and allowed for a more precise estimate

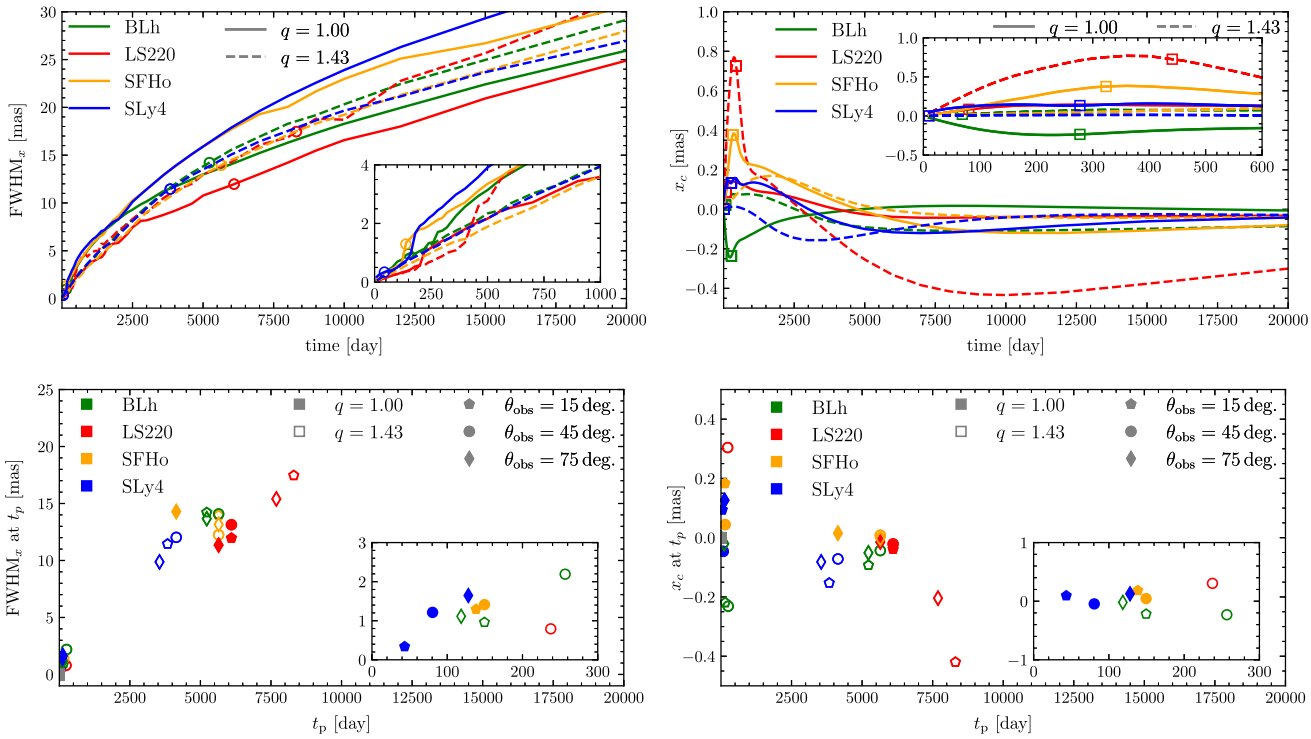

Figure 4. Time evolution of kNe afterglow sky map properties. Top left-hand panel shows the evolution of the image size, FWHM$_x$ Circular markers indicate the image size at the LC peak. Top right-hand panel shows the evolution of the flux centroid, $x_{\rm c}$ position. Square markers indicate the minimum of the LC spectral index A_ν. Bottom left panel and Bottom right panel display the image size and the position of the flux centroid at the time of the LC peak, respectively for three values of the observational angle. In each panel there is a subpanel, enlarging an early-time part of the plot. Here $n_{\rm ISM} = 0.00031$ cm^{-3}.

of the inclination angle $\theta_{\rm obs}$, was the motion of the GRB flux centroid (Mooley et al. 2018a). Here we investigate, how the presence of the kNe afterglow affects the GRB afterglow sky map $x_{\rm c}$ and FWHM$_x$ assuming that these two ejecta types do not interact. We briefly remark on this interaction in Section 3.3.

For modelling GRB afterglows, we consider the same parameters as in N22A, motivated by the analysis of GRB170817A (e.g. Hajela et al. 2019; Fernández et al. 2021), varying only the observer angle, $\theta_{\rm obs}$ and the ISM density $n_{\rm ISM}$. Specifically, we consider a Gaussian jet and with the jet half-opening angle $\theta_{\rm w} = 15^\circ$. and core half-opening angle $\theta_{\rm c} = 4.9^\circ$. The isotropic equivalent energy is $E_{\rm iso} = 10^{52}$ ergs, and the initial LF of the core is $\Gamma_{\rm c} = 300$. The microphysical parameters are set as: $\epsilon_e = 0.05$, $\epsilon_B = 0.0045$, and $p = 2.16$. Luminosity distance to the source is set to $D_{\rm L} = 41.3$ Mpc. Unless stated otherwise, we consider $\theta_{\rm obs} = 45^\circ$, and $n_{\rm ISM} = 0.00031$ cm^{-3}, as fiducial values.

In Fig. 5, we show a combined kNe plus GRB afterglow radio sky map assuming $\theta_{\rm obs} = 45^\circ$. and $t_{\rm obs} = 60$ d. At this early time the GRB afterglow is significantly brighter than the kNe one: $F^{\rm GRB}_{\nu=1\,\rm GHz} = 7.5 \times 10^{-3}$ and $F^{\rm kN}_{\nu=1\,\rm GHz} = 4 \times 10^{-4}$ mJy. However, despite being dimmer, kNe afterglow affects the properties of the total sky map significantly, shifting the position of the image flux centroid back to the centre of the explosion. Consequently, the apparent velocity computed from the motion of the flux centroid would be underestimated if the effect of kNe afterglow is not taken into account. In our case, the apparent velocity is reduced from 2.5 c to 2.1 c, at $t_{\rm obs} = 60$ d. Thus systematic underestimation of the apparent velocity may, in turn, result in overestimation of the $\theta_{\rm obs}$ or Γ. This can be understood from the following considerations. Consider, ($\theta_{\rm s} \leq \theta_{\rm obs} - \theta_{\rm s}$), where $\theta_{\rm s}$ is the average size of the extended source.

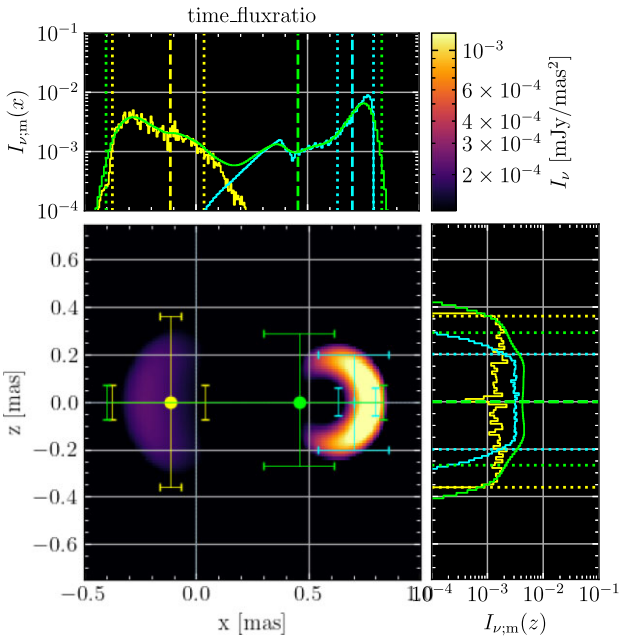

Figure 5. Combined kNe and GRB sky map. The former can be seen as a dim blob on the left, while the latter – as a bright crescent on the right. The size and the location of the flux centroid of two individual components are shown with yellow and cyan colours, respectively. The size and X_c of the combined image are shown as lime colour. As in Fig. 1 the top and right sub-panels display the z- and x-averaged brightness distributions, respectively. Sky map corresponds to $\nu_{\rm obs} = 1$ GHz, $\theta_{\rm obs} = 45^\circ$ and $t_{\rm obs} = 60$ d, $n_{\rm ISM} = 0.00031$ cm^{-3}.

There, the maximum apparent velocity $\beta_{\rm app}$ is equal to the source LF Γ, as $\theta_{\rm obs} = 1/\Gamma$. Then, assuming that the observed emission from an extended source comes predominantly from the compact region we have, $(\theta_{\rm obs} - \theta_{\rm s}) \cong 1/\beta_{\rm app}$. These arguments were used to infer Γ from radio image for GRB170817A (Mooley et al. 2018a).

Notably, at smaller observational angles, the early GRB afterglow is significantly brighter, and at $\theta_{\rm obs} \simeq 20^{\circ}$, that is generally inferred for GRB170817A, the kNe afterglow does not affect the estimated $\beta_{\rm app}$ to an appreciable degree.

At slightly later times, when the GRB afterglow reaches its peak emission we find that even for $\theta_{\rm obs} = 45^{\circ}$, the effect of the kNe afterglow on the GRB afterglow sky map properties is negligible. At the time of the GRB LC peak $t_{\rm p}^{\rm GRB} = 800$ d, the $\beta_{\rm app}$ is reduced only by $\simeq$0.1 c.

The kNe afterglow becomes important again later, when the GRB afterglow emission subsides. Numerical and semianalytic jet models show, that both prime and counter jets contribute to the late time flux (Zrake et al. 2018; Fernández et al. 2021). This forces the position of the flux centroid to move back to $x_{\rm c}^{\rm GRB} \rightarrow 0$. Before that, the jet deceleration reduces the contribution to the observed emission from the fast jet core and consequently slows down the motion of the flux centroid. The jet lateral spreading contributes to this by pushing parts of the jet to $\theta > \theta_{\rm obs}$, making them move back on the image plane. In this regard, the presence of a kNe afterglow might be confused with a more rapid lateral spreading or earlier emergence of the counter jet. *Thus, we conclude that even if the kNe afterglow does not contribute significantly to the observed total flux, it should be taken into account for accurate estimation of the jet energy and geometry from sky map observations.* Importantly, the relative brightness of two afterglows considered here depends on all free parameters of the model i.e., microphysics parameters of both shock types (relativistic and mildly relativistic), as well as the angular and velocity structure of ejecta. Moreover, the effect is most pronounced for a far-off-axis GRB and becomes negligible at observing angle much smaller than 1 rad.

Considering the available BNS merger simulations, we recall that the kNe afterglow from $q = 1$ and soft EOSs simulations is brighter, and thus it would affect the properties of the combined sky map more strongly, at least before the GRB LC peak $t_{\rm p}^{\rm GRB}$. In Fig. 6, we show the change in GRB afterglow $x_{\rm c}^{\rm GRB}$ and FWHM$_x$ in terms of how these quntities change when GRB afterglow is accompaned by the kNe afterglow,, $\Delta v = (v^{\rm GRB} - v^{\rm GRB\,\&\,kN})$ where $v \in [x_{\rm c}$, FWHM$\$_{\rm x}\$]. As expected, the general effect of the inclusion of the kNe afterglow is the decrease in $x_{\rm c}$ and, consequently, in the apparent velocity $\beta_{\rm app}$, and an increase in the image FWHM$_x$ (top right and left panels of Fig. 6). Specifically, $\Delta x_{\rm c}$ and ΔFWHM$_x$ reach $\gtrsim$1.5 and $\gtrsim -2$ mas, respectively.

At $t_{\rm p}^{\rm GRB}$ the effect of the kNe afterglow presence is minimal in all cases, as the GRB afterglow dominates the total emission and the sky map properties. *Thus, estimated at this time, image properties convey the most reliable information about the GRB afterglow.*

At higher $n_{\rm ISM}$ and $\theta_{\rm obs}$, the picture is qualitatively similar. Influence of the kNe afterglow is the most prominent at $t < t_{\rm p}^{\rm GRB}$ and for equal mass BNS simulations with soft EOS, such as SLy4 and SFHo EOSs. For $q > 1$ simulations, the maximum $\Delta x_{\rm c}$ and ΔFWHM$_x$ are about two times smaller than in $q = 1$ cases. On the other hand, at $\theta_{\rm obs} = 21.5^{\circ}$, and $n_{\rm ISM} = 0.00031$ cm^{-3}, the influence of the kNe afterglow is negligible even at $t < t_{\rm p}^{\rm GRB}$ for all simulations. In this case GRB afterglow provides a dominant contribution to the total LCs and the sky map, and the presence of kNe afterglow can only be seen at very late times $t \gg t_{\rm p}^{\rm GRB}$, when the kNe afterglow emission is coming predominantly from the non-thermal electron population. Meanwhile, in cases when the early GRB emission is beamed away, $\theta_{\rm obs} \gtrsim 45^{\circ}$, the maximum in $\Delta x_{\rm c}$ and ΔFWHM$_x$ occurs before the extreme in kNe afterglow spectral index evolution, in the regime where the emission from thermal electrons dominate the observed flux.

3.3 Effect of the GRB-modified ISM on kN afterglow sky map

In N22A we showed that when the kNe ejecta moves behind the GRB BW, it encounters an altered density profile, that we called an altered circumburst medium (CBM), and the afterglow signature changes (see also Margalit & Piran 2020). Specifically, the observed flux first decreases as most of the kNe ejecta moves subsonically behind the laterally spreading GRB BW, then increases as the kNe ejecta shocks the overdense fluid behind the GRB BW forward shock. However, the decrease and increase in the observed flux were found to be rather small: $\lesssim$ 40 and $\lesssim$ 10 per cent, respectively. The reason for this is the non-uniform nature of the kNe ejecta and finite time that GRB lateral spreading takes. Thus, different parts of the kNe ejecta encounter different regions of the altered CBM at a given time producing either an excess or a reduction in observed emission. Nevertheless, for the sake of completeness, it is worth looking at how the kNe afterglow sky map changes the altered CBM is taken into account.

In Fig. 7, we show the effect of an altered CBM on the kNe afterglow sky map for $t_{\rm obs} = 80$ d, $\theta_{\rm obs} = 60^{\circ}$, and $n_{\rm ISM} = 0.05$ cm^{-3}. The red and blue colours indicate the excess and the reduction of the observed emission with respect to the sky map computed when the altered CBM is not taken into account. As expected, the change in the observed intensity occurs primarily near poles ($z = 0$) and corresponds to kNe ejecta moving subsonically and not producing synchrotron emission. Fast elements of the kNe ejecta shocked the overdense region behind the GRB shock and produced an emission excess. Slower elements of ejecta catch up with the underdense part of the altered CBM later and this the part of the image where the emission is suppressed lies ahead of the one with emission excess. The more equatorial part of the ejecta avoids interacting with the altered CBM and, thus, its emission remains unchanged (along z-axis). The certain parts of the image, the emission excess can be significant, $(I_\nu^{\rm w}/I_\nu^{\rm w/o} \lesssim 3)$. However, combined with the emission suppression in other parts of the image, the overall emission excess is rather small. Thus, even at this relatively high $n_{\rm ISM}$ and large $\theta_{\rm obs}$ the effect of the altered CBM on the sky map properties, i.e., the position of the flux centroid and the image size are negligible.

4 DISCUSSION AND CONCLUSION

In this work, we considered synthetic radio images of the GRB and kNe afterglow. For the former we considered GRB170817A motivated model settings, i.e., laterally structured jet observed off-axis (Hajela et al. 2019; Fernández et al. 2021). For the latter, we considered a set of ejecta profiles from NR BNS merger simulations targeted to GW170817, i.e., with corresponding chirp mass. For all calculations, we use the semi-analytic afterglow code PYBLASTAFTERGLOW, presented and discussed in N21 and N22A. The key aspect of the input physics is the inclusion of two electron populations behind the kNe BW shocks, that follow power-law (non-thermal electrons) and Maxwellian (thermal electrons) distributions.

The main limitation of our work is the semianalytical nature of the model we employ especially with regards to the BW lateral expansion and ejecta internal dynamics. It remains to be investigated how GRB and kNe afterglow sky maps computed with hydrodynamics numerical codes compare to ours. It is however numerically very

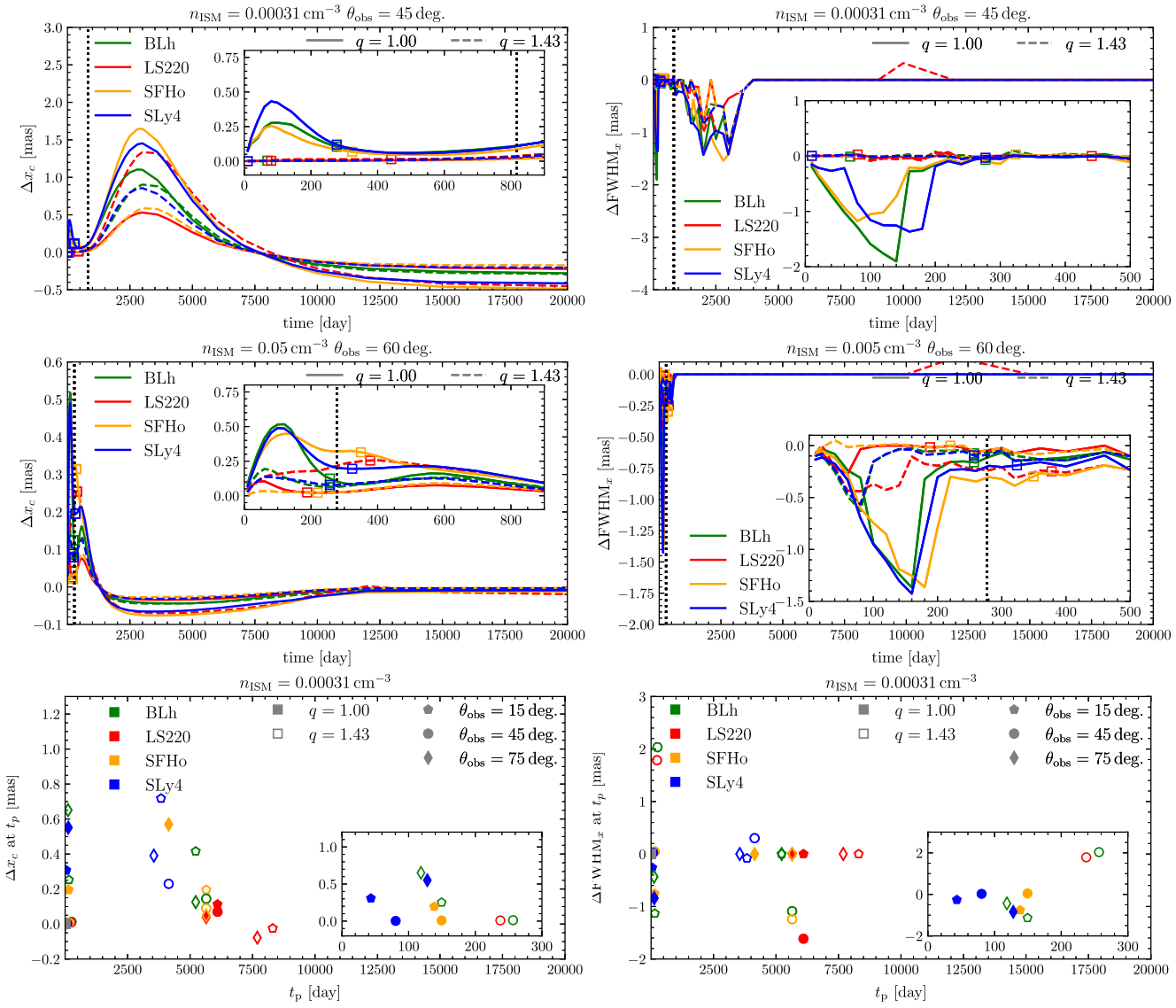

Figure 6. Top panels: time evolution of the combined sky map properties shown in terms of the difference between the value computed for the skymap that includes only GRB and the value computed for the skymap with GRB and kNe afterglows, (as shown in Fig. 5), $\Delta x_{\rm c}^{\rm GRB} = (x_{\rm c}^{\rm GRB} - x_{\rm c}^{\rm GRB\,\&\,kN})$, $\Delta{\rm FWHM}_x^{\rm GRB} = {\rm FWHM}_x^{\rm GRB} - {\rm FWHM}_x^{\rm GRB\,\&\,kN}$ on the left-hand and right-hand panels, respectively. Dashed grey line corresponds to the time of the GRB LC peak. Bottom panels: properties of the combined sky map extracted at the time of the kNe afterglow LC peak. Different colours correspond to various EOSs. Filled and empty markers indicate $q = 1.00$ and $q = 1.43$ simulations, respectively. Different markers correspond to various observing angles. In all panels, an inner sub-panel serves to enlarge the early time part of the figure.

challenging to perform such simulations on a temporal and spatial scales discussed in this work, as well as, to perform them for various possible choices of the model free parameters and kNe ejecta profiles.

The aforementioned limitations notwithstanding, we find that the kNe afterglow sky map at early times resemble a wheel or a doughnut due to the emission from thermal electrons enhanced by relativistic effects, dominating the observed flux. At later times, the sky map is largely spherical with a remaining ring structure reflecting the (a) assumed axial symmetry and (b) initial ejecta velocity distribution. The image size evolves monotonically, albeit not smoothly, reaching $\simeq 10$ mas at 3000 d and $\simeq$25 mas at 20000 d. If the kNe afterglow LC at its peak is dominated by the emission from thermal electrons, the image size is smaller reaching $\lesssim$5 mas. Thus, the properties of the fast ejecta tail can be inferred from the sky map size and its evolution.

Despite asymmetry in ejecta velocity distribution, however, the position of the image flux centroid $x_{\rm c}$ does not deviate much from 0, and is the largest ($|x_{\rm c}| < 0.4$ mas) at early times, in cases when the emission from thermal electrons dominates the observed flux. Notably, however, the asymmetry can lead to the negative values of $|x_{\rm c}|$ (assuming more on-axis observers), which if observed might hint at the equatorial nature of the fast ejecta tail.

Crucially, the presence of the kNe ejecta can affect the GRB afterglow sky map to an appreciable degree even if the former does not appreciably contribute to the total observed flux. For that to occur, however, the source must be observed sufficiently off-axis so that the early GRB afterglow emission is beamed away, while the kNe afterglow emission, dominated at this time by the emission from thermal electrons, is instead beamed more toward an observer. Specifically, at $t_{\rm obs} = 80$ d and assuming $\theta_{\rm obs} = 45^\circ$. the change in

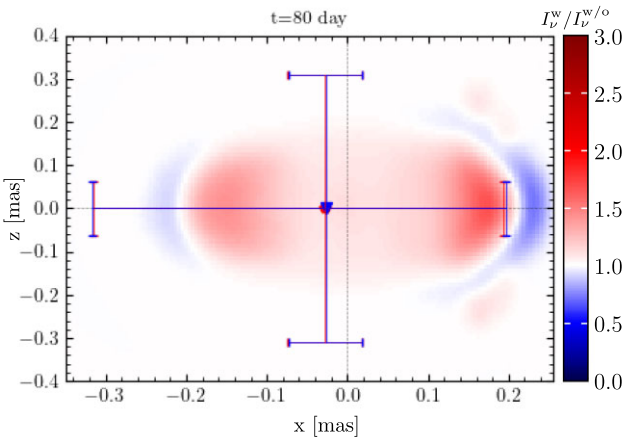

Figure 7. The ratio between two kNe afterglow sky maps with the only difference between them being is whether the CBM, altered by a passage of GRB BWs, is taken into account ($I_\nu^{\rm w}$) or not ($I_\nu^{w/o}$). Image size and the position of the flux centroid are shown as before with error bars and markers with blue colour for 'w' case and red for 'w/o' case. Sky maps are computed assuming $\nu_{\rm obs} = 1$ GHz, $\theta_{\rm obs} = 60^\circ$, and $n_{\rm ISM} = 0.05$ cm^{-3}.

the inferred value of the apparent velocity $\beta_{\rm app}$ can reach 0.5 c. At smaller $\theta_{\rm obs}$ the kNe afterglow effects the GRB afterglow sky map properties significantly less and at $\theta_{\rm obs} \simeq 20^\circ$. we find the effect to be negligible. Importantly, the relative brightness between these two types of afterglow depends on their respective sets of free parameters that are largely unconstrained. It is thus important to conduct a more thorough statistical analysis of the combined parameter space to assess the upper and lower limits of the degree to which the kNe afterglow influences the combined sky map properties.

The detectability of the kNe and GRB sky maps with next generation VLA, which is currently in the development, will be discussed in a separate study by Eddins et. al. (in preparation). Overall, in order for kNe afterglow itself to be detectable, the flux density at the LC peak should be $\gtrsim 5 \times 10^{-3}$ mJy in radio (Kathirgamaraju, Giannios & Beniamini 2019b). For BNS merger simulations considered here, this is only possible at sufficiently high density, $n_{\rm ISM} \gtrsim 0.005$ cm^{-3} at $D_{\rm L} \simeq 40$ Mpc. In order to distinguish GRB and kNe afterglows, the $\theta_{\rm obs}$ should be much larger than the jet opening angle (e.g., see figure 9 in N22A). In general, however, the detection of kNe afterglow may only be possible either before a far-off-axis GRB afterglow or long after GRB afterglow LC peak.

At such late times, and at large $\theta_{\rm obs}$, the change in the position of the sky map flux centroid due to the presence of the kNe afterglow may theoretically become detectable. It is, however, difficult to resolve a skymap at these late times with any reasonable integration time, taken into account observational noise and instrument uncertanties.

ACKNOWLEDGEMENTS

The simulations were performed on the national supercomputer HPE Apollo Hawk at the High Performance Computing (HPC) Center, Stuttgart (HLRS), under the grant no. GWanalysis/44189, and on the GCS Supercomputer SuperMUC at Leibniz Supercomputing Centre (LRZ) [project pn29ba].

We would like to thank Alessandra Corsi and Avery Eddins for the meaningfull discussions.

Software: We are grateful to the countless developers contributing to open source projects that was used in the analysis of the simulation results of this work: NUMPY (Harris et al. 2020), MATPLOTLIB (Hunter 2007), and SCIPY (Virtanen et al. 2020).

DATA AVAILABILITY:

The data sets generated during and/or analysed during the current study are available from the corresponding author on reasonable request.

REFERENCES

Abbott B. P., et al., 2017a, Phys. Rev. Lett., 119, 161101
Abbott B. P., et al., 2017b, ApJ, 848, L13
Abbott B. P., et al., 2019a, Phys. Rev., 9, 011001
Abbott B. P., et al., 2019b, Phys. Rev., 9, 031040
Ajello M. et al., 2016, ApJ, 819, 44
Alexander K. D., et al., 2017, ApJ, 848, L21
Alexander K., et al., 2018, ApJ, 863, L18
Arcavi I. et al., 2017, Nature, 551, 64
Bauswein A., Goriely S., Janka H.-T., 2013, ApJ, 773, 78
Beloborodov A. M., Lundman C., Levin Y., 2020, ApJ, 897, 141
Bernuzzi S., 2020, Gen. Rel. Grav., 52, 108
Bietenholz M. F., De Colle F., Granot J., Bartel N., Soderberg A. M., 2014, MNRAS, 440, 821
Boutelier T., Henri G., Petrucci P. O., 2011, MNRAS, 418, 1913
Bradley Cenko S., et al., 2015, ApJ, 803, L24
Coughlin M. W., Dietrich T., Margalit B., Metzger B. D., 2019, MNRAS, 489, L91
Coulter D. A., et al., 2017, Science, 358, 1556
Cowperthwaite P. S., et al., 2017, ApJ, 848, L17
Dalal N., Griest K., Pruet J., 2002, ApJ, 564, 209
Desai D., Metzger B. D., Foucart F., 2019, MNRAS, 485, 4404
Dessart L., Ott C., Burrows A., Rosswog S., Livne E., 2009, ApJ, 690, 1681
Dietrich T., Ujevic M., 2017, Class. Quant. Grav., 34, 105014
Dietrich T., Coughlin M. W., Pang P. T. H., Bulla M., Heinzel J., Issa L., Tews I., Antier S., 2020, Science, 370, 1450
Drout M. R. et al., 2017, Science, 358, 1570
Evans P. A. et al., 2017, Science, 358, 1565
Fahlman S., Fernández R., 2018, ApJ, 869, L3
Fernández R., Quataert E., Schwab J., Kasen D., Rosswog S., 2015, MNRAS, 449, 390
Fernández R., Tchekhovskoy A., Quataert E., Foucart F., Kasen D., 2019, MNRAS, 482, 3373
Fernández J. J., Kobayashi S., Lamb G. P., 2021, MNRAS, 509, 395
Fong W. et al., 2017, ApJ, 848, L23
Fujibayashi S., Kiuchi K., Nishimura N., Sekiguchi Y., Shibata M., 2018, ApJ, 860, 64
Fujibayashi S., Shibata M., Wanajo S., Kiuchi K., Kyutoku K., Sekiguchi Y., 2020, Phys. Rev. D, 101, 083029
Fujibayashi S., Kiuchi K., Wanajo S., Kyutoku K., Sekiguchi Y., Shibata M., 2023, ApJ, 942, 39
Gal-Yam A. et al., 2006, ApJ, 639, 331
Ghirlanda G., et al., 2019, Science, 363, 968
Gill R., Granot J., 2018, MNRAS, 478, 4128
Granot J., Miller M. A., Piran T., Suen W.-M., Hughes P. A., 2001, in Enrico C., Filippo F., Jens H., eds, Gamma-ray Bursts in the Afterglow Era
Granot J., Panaitescu A., Kumar P., Woosley S. E., 2002, ApJ, 570, L61
Granot J., Ramirez-Ruiz E., Loeb A., 2004, ApJ, 618, 413
Hajela A. et al., 2019, ApJ, 886, L17
Hajela A. et al., 2022, ApJ, 927, L17
Hallinan G. et al., 2017, Science, 358, 1579
Harris C. R. et al., 2020, Nature, 585, 357
Hotokezaka K., Piran T., 2015, MNRAS, 450, 1430
Hotokezaka K., Kiuchi K., Kyutoku K., Muranushi T., Sekiguchi Y.-i., Shibata M., Taniguchi K., 2013a, Phys. Rev. D, 88, 044026
Hotokezaka K., Kiuchi K., Kyutoku K., Okawa H., Sekiguchi Y.-i., Shibata M., Taniguchi K., 2013b, Phys. Rev. D, 87, 024001

Hotokezaka K., Kiuchi K., Shibata M., Nakar E., Piran T., 2018, ApJ, 867, 95
Huang Y.-J. et al., 2020, ApJ, 897, 69
Hunter J. D., 2007, Comput. Sci. Eng., 9, 90
Just O., Bauswein A., Pulpillo R. A., Goriely S., Janka H. T., 2015, MNRAS, 448, 541
Kasen D., Badnell N. R., Barnes J., 2013, ApJ, 774, 25
Kasen D., Fernández R., Metzger B., 2015, MNRAS, 450, 1777
Kasliwal M. M., et al., 2017, Science, 358, 1559
Kathirgamaraju A., Tchekhovskoy A., Giannios D., Barniol Duran R., 2019a, MNRAS, 484, L98
Kathirgamaraju A., Giannios D., Beniamini P., 2019b, MNRAS, 487, 3914
Kawaguchi K., Shibata M., Tanaka M., 2018, ApJ, 865, L21
Knoll G. F., 2000, Radiation Detection and Measurement, 3rd ed., John Wiley and Sons, New York, p. 816
Krüger C. J., Foucart F., 2020, Phys. Rev. D, 101, 103002
Kulkarni S., 2005, Modeling supernova-like explosions associated with gamma-ray bursts with short durations
Kumar P., Panaitescu A., 2000, ApJ, 541, L51
Lamb G. P., Kobayashi S., 2017, MNRAS, 472, 4953
Lamb G. P., Mandel I., Resmi L., 2018, MNRAS, 481, 2581
Lattimer J. M., Schramm D. N., 1974, ApJ, 192, L145
Levinson A., Ofek E., Waxman E., Gal-Yam A., 2002, ApJ, 576, 923
Li L.-X., Paczynski B., 1998, ApJ, 507, L59
Lyman J. D. et al., 2018, Nature Astron., 2, 751
Margalit B., Piran T., 2020 495 4 Mon. Not. Roy. Astron. Soc. aa
Margalit B., Quataert E., 2021, ApJ, 923, L14
Margutti R. et al., 2018, ApJ, 856, L18
Martin D., Perego A., Arcones A., Thielemann F.-K., Korobkin O., Rosswog S., 2015, ApJ, 813, 2
Mesler R. A., Pihlström Y. M., 2013, ApJ, 774, 77
Mesler R. A., Pihlström Y. M., Taylor G. B., Granot J., 2012, ApJ, 759, 4
Metzger B. D., 2020, Living Rev. Rel., 23, 1
Metzger B. D., Fernández R., 2014, MNRAS, 441, 3444
Metzger B. D. et al., 2010, MNRAS, 406, 2650
Metzger B. D., Bauswein A., Goriely S., Kasen D., 2015, MNRAS, 446, 1115
Metzger B. D., Thompson T. A., Quataert E., 2018, ApJ, 856, 101
Miller J. M. et al., 2019, Phys. Rev. D, 100, 023008
Moderski R., Sikora M., Bulik T., 2000, ApJ, 529, 151
Mooley K. P. et al., 2018a, Nature, 561, 355
Mooley K. P., et al., 2018b, ApJ, 868, L11
Mooley K. P., Anderson J., Lu W., 2022, Nature, 610, 273
Nakar E., 2020, Phys. Rept., 886, 1
Nakar E., Piran T., 2003, New Astron., 8, 141
Nakar E., Piran T., 2011, Nature, 478, 82
Nakar E., Piran T., 2021, ApJ, 909, 114
Nakar E., Piran T., Granot J., 2002, ApJ, 579, 699
Nathanail A., Gill R., Porth O., Fromm C. M., Rezzolla L., 2021, MNRAS, 502, 1843
Nedora V., Bernuzzi S., Radice D., Perego A., Endrizzi A., Ortiz N., 2019, ApJ, 886, L30
Nedora V., Radice D., Bernuzzi S., Perego A., Daszuta B., Endrizzi A., Prakash A., Schianchi F., 2021a, MNRAS, 506, 5908 (N21)
Nedora V. et al., 2021b, ApJ, 906, 98
Nedora V., Dietrich T., Shibata M., Pohl M., Menegazzi L. C., 2022a, MNRAS, (N22a)
Nedora V. et al., 2022b, Class. Quant. Grav., 39, 015008
Nicholl M. et al., 2017, ApJ, 848, L18
Nynka M., Ruan J. J., Haggard D., Evans P. A., 2018, ApJ, 862, L19
Ozel F., Psaltis D., Narayan R., 2000, ApJ, 541, 234
Panaitescu A., Meszaros P., 1999, ApJ, 526, 707
Perego A., Rosswog S., Cabezon R., Korobkin O., Kaeppeli R. , Arcones A., Liebendörfer M., 2014, MNRAS, 443, 3134
Perego A., Radice D., Bernuzzi S., 2017, ApJ, 850, L37
Perego A., Bernuzzi S., Radice D., 2019, Eur. Phys. J., 55, 124
Perna R., Loeb A., 1998, ApJ, 509, L85
Pihlstrom Y. M., Taylor G. B., Granot J., Doeleman S., 2007, ApJ, 664, 411
Piran T., Nakar E., Rosswog S., 2013, MNRAS, 430, 2121
Radice D., Galeazzi F., Lippuner J., Roberts L. F., Ott C. D., Rezzolla L., 2016, MNRAS, 460, 3255
Radice D., Perego A., Hotokezaka K., Bernuzzi S., Fromm S. A., Roberts L. F., 2018a, ApJ, 869, L35
Radice D., Perego A., Hotokezaka K., Fromm S. A., Bernuzzi S., Roberts L. F., 2018b, ApJ, 869, 130
Radice D., Bernuzzi S., Perego A., 2020, Annu. Rev. Nucl. Part. Sci., 70, 95
Ramirez-Ruiz E., Madau P., 2004, ApJ, 608, L89
Ramirez-Ruiz E., Granot J., Kouveliotou C., Woosley S. E., Patel S. K., Mazzali P. A., 2005, ApJ, 625, L91
Rau A., Greiner J., Schwarz R., 2006, A&A, 449, 79
Rhoads J. E., 1997, ApJ, 487, L1
Rhoads J. E., 2003, ApJ, 591, 1097
Roberts L. F., Kasen D., Lee W. H., Ramirez-Ruiz E., 2011, ApJ, 736, L21
Rosswog S., 2005, ApJ, 634, 1202
Rosswog S., Liebendoerfer M., Thielemann F., Davies M., Benz W., Piran T., 1999, A&A, 341, 499
Ruan J. J., Nynka M., Haggard D., Kalogera V., Evans P., 2018, ApJ, 853, L4
Ryan G., van Eerten H., Piro L., Troja E., 2020, ApJ, 896, 166
Sari R., Piran T., Halpern J., 1999, ApJ, 519, L17
Savchenko V., et al., 2017, ApJ, 848, L15
Sekiguchi Y., Kiuchi K., Kyutoku K., Shibata M., 2015, Phys. Rev. D, 91, 064059
Sekiguchi Y., Kiuchi K., Kyutoku K., Shibata M., Taniguchi K., 2016, Phys. Rev. D, 93, 124046
Shibata M., Hotokezaka K., 2019, Annu. Rev. Nucl. Part. Sci., 69, 41
Siegel D. M., Metzger B. D., 2017, Phys. Rev. Lett., 119, 231102
Smartt S. J., et al., 2017, Nature, 551, 75
Soares-Santos M., et al., 2017, ApJ, 848, L16
Soderberg A. M., Nakar E., Kulkarni S. R., 2006, ApJ, 638, 930
Tanaka M., Hotokezaka K., 2013, ApJ, 775, 113
Tanaka M. et al., 2017, PASJ, 69, 16
Tanvir N. R., et al., 2017, ApJ, 848, L27
Taylor G. B., Frail D. A., Berger E., Kulkarni S. R., 2004, ApJ, 609, L1
Taylor G. B., Momjian E., Pihlstrom Y., Ghosh T., Salter C., 2005, ApJ, 622, 986
Totani T., Panaitescu A., 2002, ApJ, 576, 120
Troja E. et al., 2017, Nature, 551, 71
Villar V. A., et al., 2017, ApJ, 851, L21
Vincent T., Foucart F., Duez M. D., Haas R., Kidder L. E., Pfeiffer H. P., Scheel M. A., 2020, Phys. Rev. D, 101, 044053
Virtanen P. et al., 2020, Nature Methods, 17, 261
Wanajo S., Sekiguchi Y., Nishimura N., Kiuchi K., Kyutoku K., Shibata M., 2014, ApJ, 789, L39
Winkler C., Diehl R., Ubertini P., Wilms J., 2011, Space Sci. Rev., 161, 149
Woods E., Loeb A., 1999, ApJ, 523, 187
Wu M.-R., Fernández R., Martínez-Pinedo G., Metzger B. D., 2016, MNRAS, 463, 2323
Zappa F., Bernuzzi S., Radice D., Perego A., 2022, Mon. Not. Roy. Astron. Soc., 520, 1481
Zrake J., Xie X., MacFadyen A., 2018, ApJ, 865, L2

This paper has been typeset from a TEX/LATEX file prepared by the author.